

Recoverable gas from hydrate-bearing sediments: Pore network model simulation and macroscale analyses

Jaewon Jang¹ and J. Carlos Santamarina¹

Received 12 July 2010; revised 23 April 2011; accepted 4 May 2011; published 6 August 2011.

[1] The volume of hydrate expands into a significantly larger volume of water and gas upon dissociation. Gas recovery and capillary-trapped residual gas saturation are investigated by simulating hydrate dissociation within pore networks. A fluid pressure-controlled boundary condition is used to determine the amount of recovered gas as a function of volume expansion; in this form, results are applicable to gas production by either thermal stimulation or depressurization when production rates prevent secondary hydrate or ice formation. Simulation results show that gas recovery is proportional to gas expansion, initial hydrate saturation, and the sediment pore size distribution (i.e., capillary pressure). Gas recovery is not affected by pore size in coarse-grained sediments with pores larger than 1 μm . Hydrate-bearing sediments with low hydrate saturation yield low gas recovery. Macroscale close form solutions, validated using the numerical results, provide estimates for recoverable gas as a function of the initial hydrate saturation and the fluid expansion factor.

Citation: Jang, J., and J. C. Santamarina (2011), Recoverable gas from hydrate-bearing sediments: Pore network model simulation and macroscale analyses, *J. Geophys. Res.*, 116, B08202, doi:10.1029/2010JB007841.

1. Introduction

[2] Hydrate formation is controlled by pressure, temperature, fluid chemistry and the availability of hydrate-forming gases. In sediments, hydrate distribution and saturation are also determined by the sediment pore size distribution, connectivity, and spatial variability [Waite *et al.*, 2009].

[3] Pressure-temperature P - T conditions for several hydrate-bearing reservoirs are plotted in Figure 1. In each case, the potential hydrate-bearing sediment is bounded by the reported seafloor P - T conditions on the left and the methane hydrate phase boundary on the right (shown for 3.5% salinity). The local geothermal gradient determines the slope of dotted lines that represent each formation. The superimposed thick lines show hydrate-bearing layers inferred from pore fluid chemistry, electrical resistivity logs, gamma ray logs, and wave velocity data. These results confirm that hydrates are not necessarily found throughout the gas hydrate stability zone, and sometimes the presence of hydrates is restricted to specific layers (e.g., Mt. Elbert and Gulf of Mexico).

[4] We note that hydrate saturation S_h and grain size distribution vary widely among hydrate-bearing reservoirs or even within a given borehole: gas hydrate-bearing sands in the Nankai Trough and Gulf of Mexico may reach up to 80% saturation whereas gas hydrates in fine-grained sedi-

ments often contain low hydrate saturation [Uchida *et al.*, 2004; Boswell *et al.*, 2009; Tréhu *et al.*, 2004]. The mean grain size of hydrate-bearing sediments ranges from 2 μm to 5 μm for Blake Ridge and Hydrate Ridge to 0.1 mm to 0.3 mm for the Nankai Trough and Mallik [Soga *et al.*, 2007]. Hydrates can be found filling pores typically in coarse-grained sediments, or in veins and lenses typically in fine-grained sediments [Waite *et al.*, 2009].

[5] Several numerical simulators have been developed to analyze gas production from hydrate-bearing sediments [Wilder *et al.*, 2008; Anderson *et al.*, 2011; Hong and Pooladi-Darvish, 2003; Uddin *et al.*, 2008; Nazridoust and Ahmadi, 2007; Gamwo and Liu, 2010; Moridis *et al.*, 2007; Moridis and Sloan, 2007; Moridis *et al.*, 2011; Kurihara *et al.*, 2009]. Most simulators consider mixed fluid conditions, adopt van Genuchten-type relative permeability models, and capture the thermodynamics of hydrate dissociation to estimate gas and water production rates. However, it is difficult to extract prevailing trends and to identify governing process from these simulations given their complexity and the large number of both physical and fitting parameters involved. In addition, the relative permeability models that are used were derived for an invading gas phase that percolates from the boundary as in a drying unsaturated soil: however, hydrate dissociation implies the formation of a gas phase within the medium. We also note that back-analyzed field cases are based on cumulative recovered gas at the boundary, and complete dissociation is not necessarily attained within the medium [Anderson *et al.*, 2011; Moridis *et al.*, 2011, 2007; Konno *et al.*, 2010; Hong and Pooladi-Darvish, 2003]. Hence, recoverable gas cannot be properly determined in these cases.

¹School of Civil and Environmental Engineering, Georgia Institute of Technology, Atlanta, Georgia, USA.

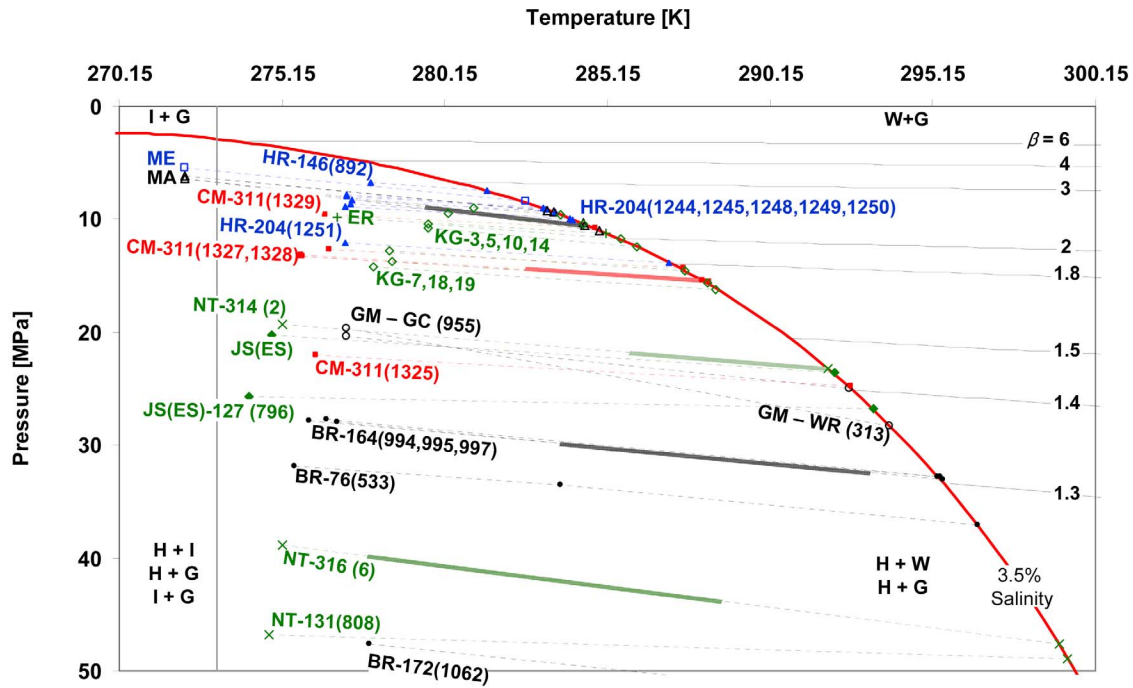


Figure 1. Pressure and temperature condition for worldwide hydrate reservoirs (to the left of the phase boundary). Lines of equal hydrate-to-fluid expansion factor $\beta = (V_g + V_w)/V_h$ are shown to the right (see section 2 for the derivation of the expansion factor β). Plotted cases correspond to (solid circle) Blake Ridge BR [Collett and Ladd, 2000; Shipboard Scientific Party, 1996a, 1996b, 1996c, 1998], (cross) Nankai Trough NT [Expedition 314 Scientists, 2009; Expedition 316 Scientists, 2009; Shipboard Scientific Party, 1991; Tobin et al., 2009a, 2009b], (green solid diamond) Sea of Japan (East Sea) JS(ES) [Shipboard Scientific Party, 1990a, 1990b; Moridis et al., 2009; Lee et al., 2010], (red solid square) Northern Cascadia Margin CM [Shipboard Scientific Party, 1994a; Expedition 311 Scientists, 2006], (open circle) Gulf of Mexico GM [McConnell et al., 2010a, 2010b], (green open diamond) Krishna-Godavari Basin (India) KG [Collett et al., 2007], (blue triangle) Hydrate Ridge HR [Shipboard Scientific Party, 1994b, 2003a, 2003b], (plus) Eel River Basin (California) ER [Shipboard Scientific Party, 1997], (open triangle) Mallik MA [Wright et al., 1999], and (blue open square) Mt. Elbert ME [Dai et al., 2011] (Hydrate zone only below permafrost is considered here). The methane hydrate phase transformation boundary is shown for 3.5% salinity water [Sloan and Koh, 2008]. The modified Peng-Robinson equation of state [Stryjek and Vera, 1986] is used to calculate fluid expansion. We assume no solubility of methane gas in water, constant mass density for water, and no capillary effects, i.e., coarse grains.

[6] In this manuscript, we use pore network models defined with a minimal set of physically meaningful pore-scale parameters to elucidate gas recovery and water production as a function of the initial hydrate saturation, pore size distribution, and P - T conditions. First, we compute fluid volume expansion during hydrate dissociation and gas recovery as a function of in situ P - T conditions and anticipated P - T changes. Then, we evaluate the effect of fluid expansion, initial hydrate saturation and pore size distribution on recoverable gas and on the evolution of gas saturation during hydrate dissociation and subsequent depressurization. Results are applicable to gas production by either depressurization or thermal stimulation when production rates prevent secondary hydrate or ice formation.

2. Preliminary Analyses: Fluid Expansion

[7] Hydrates dissociate into methane-saturated water and water-saturated methane gas. There is a pronounced pressure dependent fluid expansion across the phase boundary

during hydrate dissociation, followed by additional gas expansion due to depressurization.

[8] Let's derive an expression for fluid expansion as a function of reservoir P - T conditions and pore throat size. Since the solubility of methane in water is very low, it can be neglected for first order estimation of fluid expansion. We define the fluid expansion factor associated with hydrate dissociation β as the ratio of the combined gas and water volumes (V_g and V_w respectively) to the initial volume of hydrate V_h , so that $\beta = (V_g + V_w)/V_h$. The dissociated methane volume V_g is a function of P - T conditions; we use the modified Peng-Robinson equation of state (PRSV) to relate V_g to P_g and T_g [Stryjek and Vera, 1986]:

$$P_g = \frac{RT_g}{V_g - b} - \frac{a}{V_g(V_g + b) + b(V_g - b)} \quad (1)$$

The values of a and b parameters for methane gas and the universal gas constant R are summarized in Table 1.

Table 1. Parameters Used in the Equation of State^a

Parameter	Symbol	Value
Universal gas constant	R	83.15 [bar · cm ³ /mol·K]
Attraction term parameter	a	$(0.457235R^2T_c^2/P_c)\alpha$
Repulsion term parameter	b	$0.077796RT_c/P_c$
	α	$[1 + \kappa(1 - T_r^{0.5})]^2$
Adjustable parameter	κ	$\kappa_0 + \kappa_1(1 + T_r^{0.5})(0.7 - T_r)$
Adjustable parameter	κ_0	$0.378893 + 1.4897153\omega$
		$- 0.17131848\omega^2 + 0.0196544\omega^3$
Adjustable parameter	κ_1	-0.00159 for methane
Acentric factor	ω	0.01045 for methane
Critical pressure	P_c	4.595 MPa for methane
Critical temperature	T_c	190.555 K for methane
Reduced temperature	T_r	T/T_c

^aStryjek and Vera [1986].

[9] Gas and water are at different pressures in a porous medium. The capillary pressure P_c is the pressure difference between gas P_g and water P_w pressures. It is a function of surface tension Γ , contact angle θ , and pore throat radius R_{th} :

$$P_c = P_g - P_w = \frac{2\Gamma \cos(\theta)}{R_{th}} \quad (2)$$

The volume of water V_w that results from hydrate dissociation is related to the initial volume of hydrate V_h as $V_w/V_h = (18\chi)/(16 + 18\chi) \cdot \rho_h/\rho_w$ where χ is the hydration number; for a theoretical value of $\chi = 5.75$, then $V_w = 0.79V_h$. The molar concentration of methane in hydrate is λV_h where λ is the amount of methane per unit volume of hydrate ($\lambda = \rho_h/(16 + 18\chi)$ and equals $\lambda = \rho_h/(119.5 \text{ g/cm}^3)$ [mol/cm³] when $\chi = 5.75$). Combining these expressions, the fluid expansion factor β can be written as

$$\beta = \frac{V_g + V_w}{V_h} = \frac{V_g}{V_h} + \frac{V_w}{V_h} = f(P_w, P_c, T_g) + \frac{18\chi}{16 + 18\chi} \frac{\rho_h}{\rho_w} \quad (3)$$

The full equation for β is used in subsequent computations but it is not included in the text given its complexity (the volume of gas V_g is obtained by solving a cubic equation (equation (1)).

[10] A simple expression for the fluid expansion factor β can be obtained using the “modified ideal gas law”:

$$\begin{aligned} \beta &= \frac{V_g + V_w}{V_h} \\ &= \frac{z\lambda RT_g}{P_g} + \frac{18\chi}{16 + 18\chi} \frac{\rho_h}{\rho_w} \\ &= \frac{z\lambda RT_g}{P_w + \frac{2\Gamma}{R_{th}} \cos \theta} + \frac{18\chi}{16 + 18\chi} \frac{\rho_h}{\rho_w} \end{aligned} \quad (4)$$

where λ is the amount of methane per unit volume of hydrate and z is a “compression factor” added to the ideal gas law to fit the PRSV equation within the P - T range of interest. For $z = 0.7$, the expansion factor calculated with equation (4) closely matches the factor computed with the modified Peng-Robinson equation of state (equation (3)). This simple and explicit close form expression for the fluid expansion factor β highlights the interplay between pressure, temperature, surface tension, and pore throat radius.

[11] Lines of equal hydrate-to-fluid expansion factor β are plotted in Figure 1 to the right of the phase boundary. There is a significant volume increase across the phase boundary: an initial hydrate volume V_0 immediately inside the stability field converts into βV_0 immediately outside the stability field. For example, the initial expansion is $\beta \sim 1.3$ near the bottom of the gas hydrate stability zone in Blake Ridge [Shipboard Scientific Party, 1996a, 1996b, 1996c], and $\beta \sim 2.8$ for Mt. Elbert formation. No grain size-dependent capillary effect is assumed in this case, $P_g = P_w$, therefore, trends apply to coarse, sandy sediments. The pore size dependent expansion factor $\beta = f(P_w, P_c, T_g)$ computed with the PRSV-based equation (3) is used in the following pore network model simulations.

3. Pore Network Model Simulation

[12] Let us define a pore network model as a system of pores connected by zero-volume throats (Figure 2a). Capillary pressure (equation (2)) develops at throats and determines gas pressure and fluid movement.

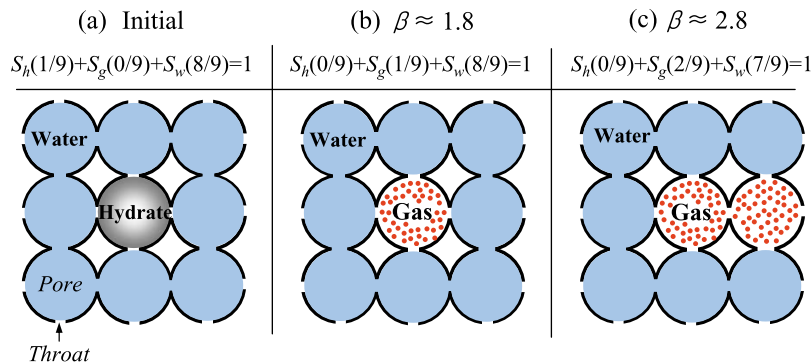


Figure 2. Pore network model configuration and evolution of gas saturation during dissociation. (a) A pore network model consists of pores interconnected by throats. Hydrate starts to dissociate and release gas when $\beta > 1$. (b) Gas occupies the initially hydrate-filled pore when $\beta \approx 1.8$. (c) Gas expands into neighboring pores as expansion increases beyond $\beta > 1.8$.

3.1. Model Parameters

[13] The size of pores is lognormally distributed with a characteristic mean pore size $\mu(R_p)$ and the standard deviation defined in terms of the natural logarithm of pore radius $\sigma(\ln(R_p/[\mu\text{m}]))$. Compiled mercury intrusion porosimetry data for a wide range of sediments suggest that $\sigma(\ln(R_p/[\mu\text{m}])) \approx 0.4 \pm 0.2$ (H. S. Phadnis and J. C. Santamarina, Pore size limited life in sediments, submitted to *Geotechnique Letters*, 2011).

[14] The size of any given throat is determined by the size of the two neighboring pores. The ratio of throat to pore size $\alpha = R_{th}/R_p$ is a function of the sediment packing geometry. For example, $\alpha = 0.565$ for simple cubic, $\alpha = 0.374$ for face-centered cubic, and $\alpha = 0.688$ for tetrahedral mono size packings [Kruyer, 1958]. Experimentally determined values are $\alpha = 0.242\sim 0.698$ for glass beads [Al-Raoush and Willson, 2005], $\alpha = 0.519$ for Berea sandstone [Øren and Bakke, 2003], $\alpha = 0.364\sim 0.520$ for Fontainebleau sandstone [Sok et al., 2002]. In this simulation, we set the throat size equal to half the size of the smaller of the two neighboring pores, $R_{th} = 0.5 \cdot \min(R_{p1}, R_{p2})$; the average value $\alpha = 0.5$ is chosen from this compilation of theoretical and experimental values. As a result, the throat size distribution is inherently correlated with the pore size distribution.

[15] The hydration number χ establishes the ratio between water and gas in a hydrate mass $\text{CH}_4 \cdot \chi \text{H}_2\text{O}$. The theoretical hydration number χ in structure I methane hydrate is $\chi = 5.75$ ($= 46/8$) [Sloan and Koh, 2008]. Slightly higher values (typically between 6.0 and 6.3) are found in natural and laboratory-made gas hydrates [Kida et al., 2009a, 2009b; Kim et al., 2005; Lu et al., 2005; Uchida et al., 1999; Ripmeester et al., 2005; Ripmeester and Ratcliffe, 1988; Sum et al., 1997; Seo et al., 2002]. The mass density of hydrates $\rho_h = 0.92 \text{g/cm}^3$ used in this study assumes full cage occupancy $\chi = 5.75$ ($8\text{CH}_4 \cdot 46\text{H}_2\text{O}$) in the unit lattice whose volume is $(\sim 12\text{Å})^3$.

[16] Capillary pressure is proportional to surface tension (equation (2)). The water-methane surface tension depends on pressure and temperature [Ren et al., 2000]. At a temperature of 25°C , it decreases from 0.07N/m to 0.06N/m as the pressure increases from 1.0MPa to 10MPa [Sachs and Meyn, 1995]. In this study, a constant surface tension $\Gamma = 0.07 \text{N/m}$ is used. The contact angle θ is assumed to be zero so that $\cos(\theta) = 1$ to represent a water-wet mineral surface.

[17] The spatially uncorrelated pore network is generated with a preselected pore size distribution. Hydrates are disseminated at random to satisfy a target initial hydrate saturation S_h . Due to Ostwald ripening, we anticipate that hydrates and water do not coexist in the same pore in natural gas hydrate-bearing sediments. Therefore, pores are fully filled with either hydrate or water in these simulations (see section 6 for a detailed discussion of this hypothesis).

3.2. Boundary Conditions

[18] A periodic boundary is used to effectively represent a large hydrate-bearing reservoir using a relatively small size $15 \times 15 \times 15$ cubic pore network. Pores on two parallel boundary faces are assumed to be connected to each other. Gas in the pore on one boundary can expand into the pore on the other parallel boundary face. Gas expansion continues with increasing expansion factor β until the gas

cluster percolates in the flow direction toward the drainage boundary. Once a gas cluster percolates, it is no longer taken into consideration for further gas expansion since it is already connected to a drainage boundary. Gas production starts when a gas cluster percolates to the boundary and increases with gas expansion.

[19] The algorithm properly captures the hindered expansion of fluids in pores due to the emergence of capillary pressure at pore throats. Water drains during gas expansion as long as water pores form a percolating path connected to the drainage boundary. If an isolated water pore develops during gas expansion, water remains in the pore and is not displaced by further gas expansion.

3.3. Hydrate Dissociation and Gas Expansion

[20] The simulation is run by gradually lowering the pressure at the boundary, i.e., pressure-controlled boundary conditions. The temperature is maintained constant during a given simulation. However, all results are plotted in terms of the expansion factor β . A given value of the expansion factor β can be reached by changes in either pressure or temperature, or both. Therefore, results in terms of β are valid for production strategies using depressurization or heating in the absence of secondary hydrate or ice formation, i.e., dissociation progresses slowly so that the rate of heat transport is much higher than the rate of heat consumption during hydrate dissociation. (Note that ice formation during gas production would change the pore size distribution and could alter results reported here.)

[21] Furthermore, we assume that there is no pressure gradient across the network given its small length scale (note the pressure gradient is considered in the work of Tsimpanogiannis and Lichtner [2006]).

[22] These assumptions allow us to anticipate the evolution of the local gas-water balance in a reservoir as a function of the fluid expansion factor β only, within the restrictions identical above. We emphasize that the gas production algorithm using pore network models does not consider dissociation kinetics and heat conduction, and cannot provide gas production rates.

[23] During early stage of dissociation, gas remains in the same pore and displaces the water produced from hydrate dissociation. Then, gas expands to invade neighboring water-filled pores if the gas pressure P_g is higher than the water pore pressure P_w in the neighboring pore plus the capillary pressure P_c at the throat connecting the gas-filled pore and its neighboring water-filled pore:

$$P_g > P_w + P_c \quad (5)$$

The gas cluster expands into neighboring water-filled pores that have the smallest combined water and capillary pressure $P_w + P_c$. As the gas expands, the gas pressure decreases.

[24] Figure 2 captures hydrate dissociation and gas expansion stage discussed above as a function of the fluid expansion factor β . Hydrates start to dissociate and release gas when $\beta > 1$ (Figure 2a). When the gas expansion factor is $\beta \approx 1.8$, the gas dissociated from hydrates fully occupies the pore which was initially filled with hydrates and has displaced the water produced by hydrate dissociation (Figure 2b). At this stage, gas saturation S_g is the same as the initial hydrate saturation S_h . Additional water drains when

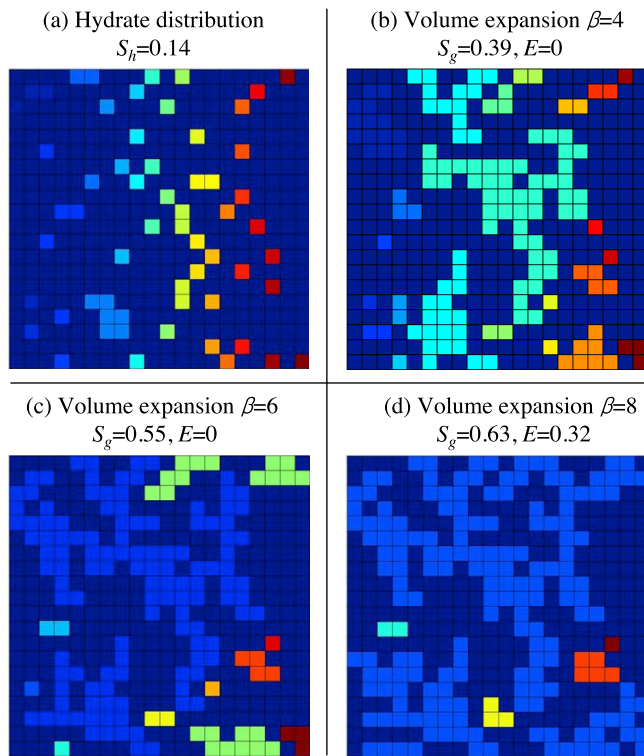


Figure 3. Initial hydrate distribution and evolution of gas saturation during hydrate dissociation and gas expansion. (a) Initial hydrate distribution for a hydrate saturation of $S_h = 15\%$; uncorrelated random distribution is assumed. (b) and (c) Gas cluster formation during gas expansion; the different colors indicate different gas clusters. (d) Percolating gas cluster (blue) after the completion of gas expansion ($\beta = 8$) is considered for the calculation of gas recovery efficiency. Two-dimensional pore network model with periodic boundary condition: 20×20 pores, randomly distributed pore radius with constant mean $\mu(R_p) = 1 \mu\text{m}$ and standard deviation $\sigma[\ln(R_p)] = 0.4$. The throat radius R_{th} between two neighboring pores is equal to half of the minimum of the two pore radii $R_{th} = 0.5 \cdot \min(R_p^1, R_p^2)$.

the gas expands to invade a neighboring water-filled pore (Figure 2c). The assessment of water pore connectivity and the identification of gas clusters are done using the Hoshen-Kopelman algorithm at every expansion step [Hoshen and Kopelman, 1976; Al-Futaisi and Patzek, 2003]. If two gas clusters expand to occupy neighboring pores, the two gas clusters coalesce and the pressure of the coalesced gas cluster is calculated with new gas cluster volume and the gas mass contained in two gas clusters.

3.4. Gas Production Evaluation

[25] Gas recovery efficiency is determined at each expansion step. The gas in clusters is under high pressure P_{g1} . As soon as the gas cluster percolates, gas is produced and the pressure in the gas cluster equalizes to the external fluid pressure P_{g2} . The recovered gas $\Delta n = n_1 - n_2$ [mol] is the difference between the gas n_2 remaining in the percolated gas cluster at pressure P_{g2} and the gas n_1 originally contained in the gas cluster at pressure P_{g1} . Gas recovery efficiency E is defined as the ratio of the recovered gas $\Delta n =$

$n_1 - n_2$ to the initial gas n_1 which is the same as the mass of methane contained in the initially available hydrate mass:

$$E = \frac{n_1 - n_2}{n_1} \quad (6)$$

The gas in isolated gas clusters is not recovered and remains within the network; the cluster gas pressure is higher than the externally imposed fluid pressure.

3.5. Cluster Visualization (in 2D)

[26] Hydrate dissociation and gas production are simulated by applying the rules and assumptions described above. To facilitate visualization, results shown in Figure 3 were obtained for a two-dimensional pore network (Note the simulation parameters are listed in the caption). Distributed hydrates dissociate, release gas, and displace water. The gas occupies the initially hydrate-filled pores as soon as hydrates dissociate (Figure 3a). Gradually, gas expands into its neighboring water pores as the expansion factor β increases (Figures 3b and 3c). Eventually, gas clusters coalesce until they percolate the pore network horizontally and gas is produced (Figure 3d). Some gas clusters cannot overcome the capillary pressure and remain trapped.

[27] Isolated water pores may be found surrounded by gas clusters. Gas clusters cannot expand into these isolated water clusters because water cannot drain. Similarly, gas clusters do not expand into neighboring water pores once gas percolates, and gas production continues from these gas clusters with the increasing expansion factor. In two-dimensional pore networks with coordination number $cn = 4$, the expansion of gas cluster is more often inhibited due to trapped water than in 3D networks. Therefore, the gas recovery efficiency in 2D pore networks is lower than in 3D simulation. In the rest of this manuscript, three-dimensional pore networks are used to compute all results (simple cubic packing, $cn = 6$).

4. Numerical Results

[28] The following results are plotted in terms of the expansion factor β to generalize their validity to gas production by either thermal stimulation or depressurization in the absence of secondary hydrate or ice formation.

4.1. Effect of Pore Network Size

[29] Pore networks of two different sizes ($15 \times 15 \times 15$ and $15 \times 15 \times 30$) are used to assess the size effect on gas recovery efficiency. The size of pore networks along the two axes transverse to the flow direction are the same (15×15), but the length along the flow direction is different (15 versus 30). Percolating gas clusters in the flow direction are considered to calculate the gas recovery efficiency. The gas recovery efficiencies computed from both pore networks of different sizes are very similar especially for higher hydrate saturation (Figure 4). At low hydrate saturation ($S_h \leq 30\%$), the efficiency obtained from long pore networks ($15 \times 15 \times 30$) is slightly smaller than that of the short pore networks ($15 \times 15 \times 15$).

4.2. Effect of Gas Expansion and Initial Hydrate Saturation

[30] Gas recovery efficiency as a function of gas expansion factor β is obtained from simulations using different

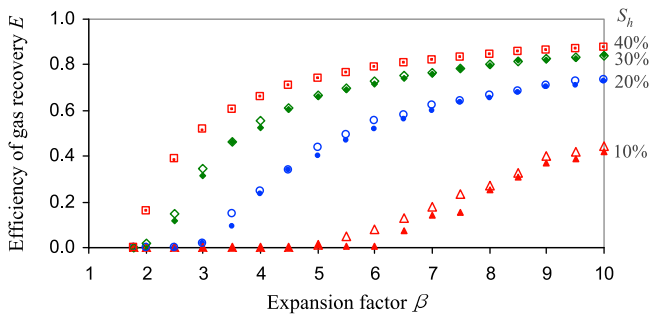


Figure 4. The effect of pore network size on computed efficiency. Each point is an average of 10 realizations. Pore network size: $15 \times 15 \times 30$ (solid) and $15 \times 15 \times 15$ (empty).

initial hydrate saturations S_h . The initial hydrate saturation varied from $S_h = 5\%$ to $S_h = 40\%$ (Figure 5; network parameters listed in the caption). Each data point in Figure 5a represents the gas recovery efficiency averaged over 20 realizations. The gas recovery efficiency E increases as the expansion factor increases at a given initial hydrate saturation, and also increases with initial hydrate saturation at a given gas expansion (Figure 5a).

[31] Figures 5b and 5c show residual and isolated gas saturation. The residual gas saturation S_g^{res} is the same as the initial hydrate saturation S_h when the gas expansion factor is $\beta \approx 1.8$ (Figure 5b, refer to Figure 2b). Gas clusters start to interconnect and form percolating gas clusters; both residual and isolated gas saturations increase with increasing gas expansion. The isolated gas saturation starts to decrease when the residual gas saturation exceeds 30–35% as most of the gas clusters are interconnected (Note the percolation threshold of 3D simple cubic arrangement $cn = 6$ is 25% [Sahimi, 1994]). Once most of the gas clusters are connected, there is not much increase in the residual gas saturation and the gas recovery efficiency markedly increases with increasing gas expansion (Figure 5). At high expansion β , the residual gas saturation converges at 40–45% for all initial S_h cases. On the other hand, the maximum isolated gas saturation is less than 30%. Notice the low isolated gas saturation when $S_h = 40\%$, even at a low expansion factor $\beta \approx 1.8$ (Figure 5c) because most of the hydrate pores are initially interconnected at such a high initial hydrate saturation.

4.3. Effect of Pore and Throat Size

[32] Throat size R_{th} (dependent of pore size R_p) defines capillary pressure (equation (2)), determines capillary gas trapping (equation (5)), and affects the gas recovery efficiency (equation (6)). Several mean pore radii $\mu(R_p) = 0.05 \mu\text{m}$, $0.1 \mu\text{m}$, $1 \mu\text{m}$, $10 \mu\text{m}$, and $100 \mu\text{m}$ with constant standard deviation in pore size $\sigma(\ln(R_p/[\mu\text{m}])) = 0.4$ are simulated while maintaining the initial hydrate saturation at $S_h = 10\%$ in all cases. Results show that the capillary pressure P_c at throats inhibits gas expansion, but its effect is not significant on recovery efficiency when the mean pore radius is larger than $1 \mu\text{m}$, $\mu(R_p) > 1 \mu\text{m}$ (Figure 6a).

Likewise, residual and isolated gas saturations are similar when $\mu(R_p) > 1 \mu\text{m}$ (Figures 6b and 6c).

[33] When $\mu(R_p) < 0.1 \mu\text{m}$, small throats cause high capillary pressure and inhibit gas expansion so that gas clusters are smaller and less connected. For example, the capillary pressure at a throat size $R_{th} = 0.05 \mu\text{m}$ is $P_c = 2.8 \text{ MPa}$ compared to $P_c = 0.14 \text{ MPa}$ at the throat of radius $R_{th} = 1 \mu\text{m}$ (see equation (2) and section 3). Therefore, simulations with small mean pore size $\mu(R_p)$ show low gas recovery efficiency even after pronounced expansion (Figure 6a). Conversely, the isolated gas saturation remains around 30% in the cases of $\mu(R_p) = 0.05$ and $0.1 \mu\text{m}$ while the isolated gas saturation in the case of larger mean pore $\mu(R_p) \geq 1 \mu\text{m}$ decreases as expansion increase (Figure 6c).

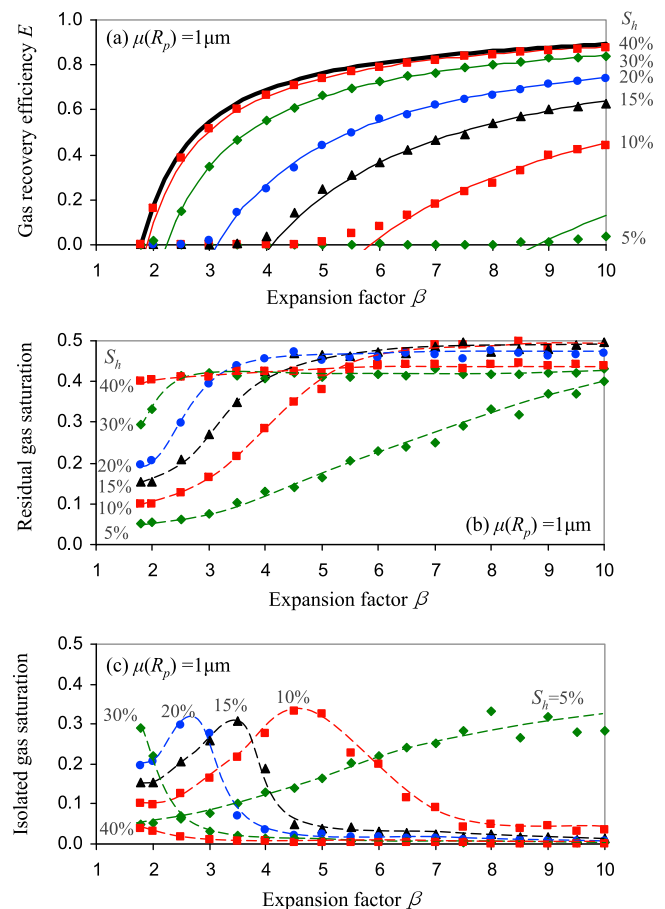


Figure 5. The effect of initial S_{hyd} . Gas recovery efficiency E , and evolution of residual and isolated gas saturation as a function of expansion factor β for different initial hydrate saturation $S_h = 5\%$, 10% , 15% , 20% , 30% and 40% . (a) Efficiency in gas recovery. (b) Residual gas saturation. (c) Isolated gas saturation. Each point is an average of 20 realizations. Three-dimensional pore network model: $15 \times 15 \times 15$ pores. Randomly distributed pore radius with constant mean $\mu(R_p) = 1 \mu\text{m}$ and standard deviation $\sigma[\ln(R_p)] = 0.4$. Pore throat $R_{th} = 0.5 \cdot \min(R_p^1, R_p^2)$. Symbols in Figures 5a–5c are numerical results, thin and thick lines in Figure 5a are the analytical model, and broken lines in Figures 5b and 5c are trend added to facilitate the visualization of numerical results.

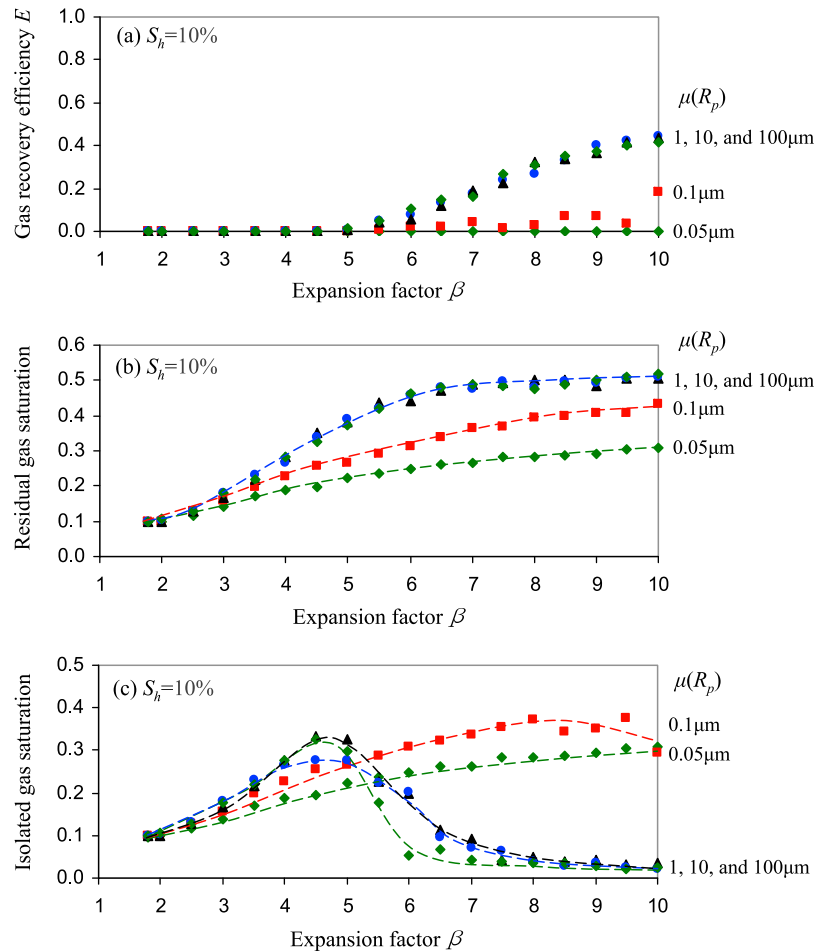


Figure 6. The effect of mean pore size. Gas recovery efficiency E , and evolution of residual and isolated gas saturation as a function of expansion factor β for various mean pore size $\mu(R_p) = 0.05, 0.1, 1, 10,$ and $100 \mu\text{m}$. Initial hydrate saturation $S_h = 15\%$. (a) Efficiency in gas recovery. (b) Residual gas saturation. (c) Isolated gas saturation. Each point is an average of 20 realizations. Three-dimensional pore network model: $15 \times 15 \times 15$ pores. Randomly distributed pore radius with constant mean $\mu(R_p) = 1 \mu\text{m}$ and standard deviation $\sigma[\ln(R_p)] = 0.4$. Pore throat $R_{th} = 0.5 \cdot \min(R_p^1, R_p^2)$. Symbols in Figures 6a–6c are numerical results; broken lines in Figures 6b and 6c are trend added to facilitate the visualization of numerical results.

4.4. Effect of Pore Size Variability

[34] The effect of pore size variability in terms of standard deviation in pore size $\sigma(\ln(R_p/[\mu\text{m}]))$ on the gas recovery efficiency is shown in Figure 7. As the standard deviation in pore size increases, the gas recovery efficiency decreases (Figure 7a). Conversely, the residual gas saturation when pore size is uniform $\sigma(\ln(R_p/[\mu\text{m}])) \rightarrow 0$ is lower than when pore size is well distributed $\sigma(\ln(R_p/[\mu\text{m}])) > 0$ (Figure 7b).

[35] These results can be understood by noting that: (1) the number of small pores increases as the standard deviation in pore size $\sigma(\ln(R_p/[\mu\text{m}]))$ increases for a constant mean pore size $\mu(R_p)$; and (2) the throat size depends on the smaller size of neighboring pores. Therefore, the mean throat size $\mu(R_{th})$ decreases as the standard deviation in pore size $\sigma(\ln(R_p/[\mu\text{m}]))$ increases (from $\mu(R_{th}) = 0.5 \mu\text{m}$ to $0.34 \mu\text{m}$ as the standard deviation changes from $\sigma(\ln(R_p/$

$[\mu\text{m}])) = 0$ to 0.6 even though the mean pore size remains constant $\mu(R_p) = 1 \mu\text{m}$).

5. Analytical Solution for Gas Recovery Efficiency

[36] Let's derive an expression for gas recovery efficiency based on macroscale concepts, but guided by pore-scale information gathered from the previous pore network simulations. Figure 8a shows the initial pore volume V_p occupied by hydrate and water in a gas-limited hydrate-bearing sediment. Figures 8b–8e show the volumes of gas and water for several production scenarios. The volume of water V_w^{dis} that results from hydrate dissociation is $V_w^{dis} = 0.79 V_h^{ini}$ where V_h^{ini} is the initial hydrate volume (for a theoretical hydration number $\chi = 5.75$; see section 2). The combined volume of gas and water from dissociation is equal to $V_g^{dis} + V_w^{dis} = \beta V_h^{ini}$. The gas recovery efficiency $E = V_g^{rec}/V_g^{dis}$ is a function of the

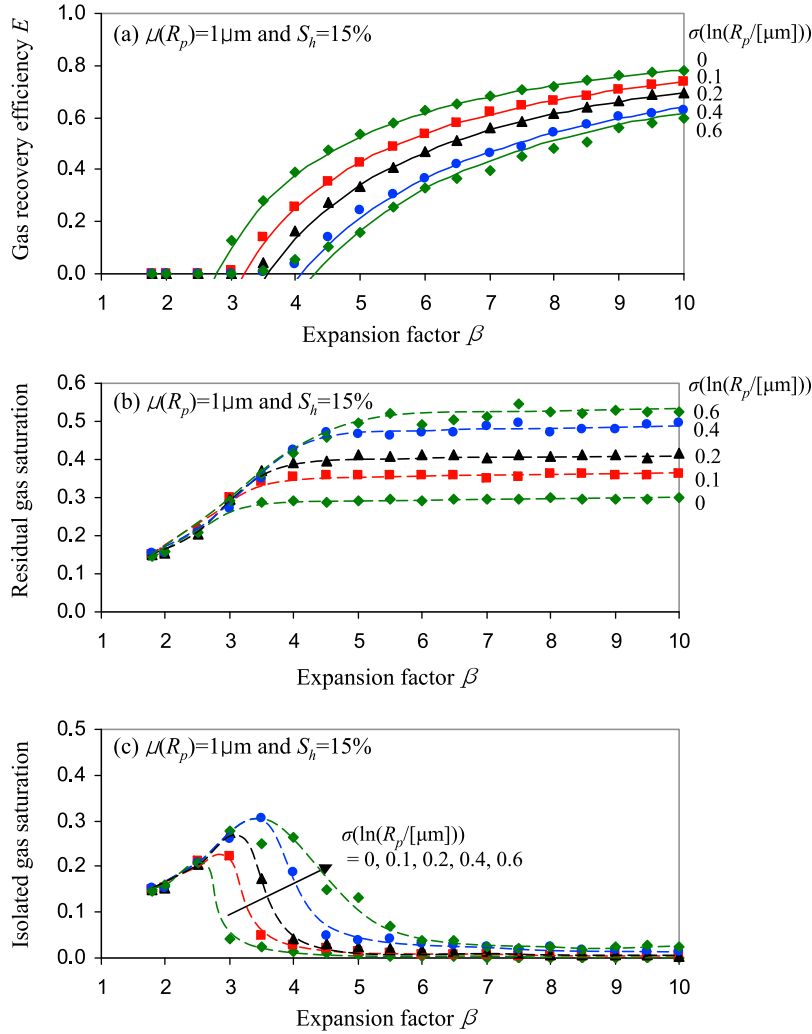


Figure 7. The effect of pore size variability. Gas recovery efficiency E , and evolution of residual and isolated gas saturation as a function of the pore size variability in terms of standard deviation for a log-normal pore size distribution: $\sigma[\ln(R_p/[\mu\text{m}])] = 0$ (uniform distribution), 0.1, 0.2, 0.4, and 0.6. Initial hydrate saturation $S_h = 15\%$. (a) Efficiency in gas recovery. (b) Residual gas saturation. (c) Isolated gas saturation. Each point is an average of 20 realizations. Three-dimensional pore network model: $15 \times 15 \times 15$ pores. Randomly distributed pore radius with constant mean $\mu(R_p) = 1 \mu\text{m}$. Pore throat $R_{th} = 0.5 \cdot \min(R_p^1, R_p^2)$. Symbols in Figures 7a–7c are numerical results, thin and thick lines in Figure 7a are the analytical model, and broken lines in Figures 7b and 7c are trend added to facilitate the visualization of numerical results.

gas expansion factor $\beta = (V_g^{dis} + V_w^{dis})/V_h^{ini}$, the residual gas saturation $S_g^{res} = V_g^{res}/V_p$, and initial hydrate saturation $S_h = V_h^{ini}/V_p$. Several production cases are analyzed next:

[37] 1. Gas displaces water (both initial and from dissociation; Figure 8b). Then, efficiency depends on residual gas saturation S_g^{res} :

$$E_1 = \frac{V_g^{rec}}{V_g^{dis}} = \frac{V_g^{dis} - V_g^{res}}{V_g^{dis}} = \frac{\beta V_h^{ini} - 0.79 V_h^{ini} - V_g^{res}}{\beta V_h^{ini} - 0.79 V_h^{ini}} = \frac{\beta - 0.79 - S_g^{res}/S_h}{\beta - 0.79} \left(0.21 S_h \leq S_g^{res} \leq 1 \right). \quad (7)$$

[38] 2. All the water (both initial V_w^{ini} and from dissociation V_w^{dis}) remain within the sediment (Figure 8c). In this

case, the residual gas saturation becomes $S_g^{res} = 1 - S_w = 1 - (S_w^{ini} + S_w^{dis}) = 1 - (1 - S_h) - 0.79 S_h = 0.21 S_h$. Then

$$E_2 = \frac{V_g^{rec}}{V_g^{dis}} = \frac{V_g^{dis} - 0.21 V_h^{ini}}{V_g^{dis}} = \frac{\beta V_h^{ini} - V_h^{ini}}{\beta V_h^{ini} - 0.79 V_h^{ini}} = \frac{\beta - 1}{\beta - 0.79} \quad (8)$$

This case could apply to a water-limited reservoir where gas percolates. Then, high gas recovery efficiency could be reached (equation (8)) because the dissociated gas is produced along the existing percolating gas path as soon as hydrates dissociate.

[39] 3. Gas displaces only the water from dissociation V_w^{dis} (Figure 8d). In this case, gas will occupy the space initially

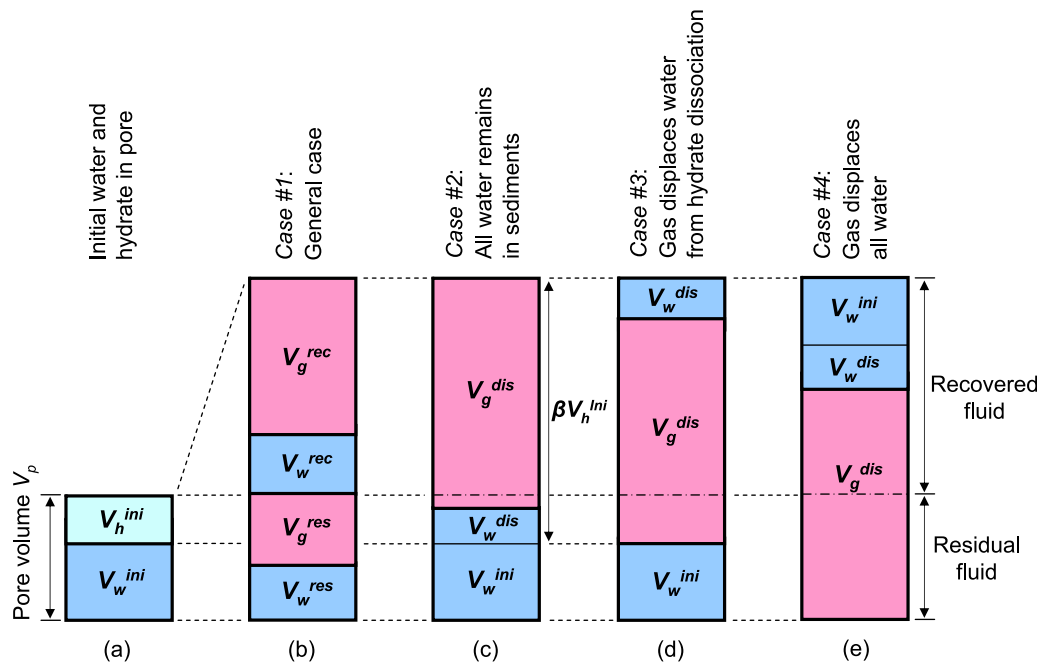


Figure 8. Macroscale analysis. Several cases of gas and water production during hydrate dissociation and gas expansion. (a) Initial hydrate and water saturation. (b) Gas displaces water and fills the pores in sediments. (c) All water remains in sediments ($S_g^{res} = 0.21S_h$). (d) Gas displaces the water from hydrate dissociation ($S_g^{res} = S_h$). (e) Gas displaces all water ($S_g^{res} = 1$).

filled with hydrate and the residual gas saturation becomes $S_g^{res} = S_h$. Then, the gas recovery efficiency is

$$E_3 = \frac{V_g^{rec}}{V_g^{dis}} = \frac{V_g^{dis} - V_h^{ini}}{V_g^{dis}} = \frac{\beta V_h^{ini} - 1.79V_h^{ini}}{\beta V_h^{ini} - 0.79V_h^{ini}} = \frac{\beta - 1.79}{\beta - 0.79}. \quad (9)$$

[40] 4. Gas displaces all water, both initial and from dissociation $V_w^{ini} + V_w^{dis}$, before gas recovery begins so that $S_g^{res} = 1$ (Figure 8e). Then

$$E_4 = \frac{V_g^{rec}}{V_g^{dis}} = \frac{V_g^{dis} - V_v}{V_g^{dis}} = \frac{\beta V_h^{ini} - V_w^{dis} - V_v}{\beta V_h^{ini} - V_w^{dis}} \\ = \frac{\beta V_h^{ini} - 0.79V_h^{ini} - V_v}{\beta V_h^{ini} - 0.79V_h^{ini}} = \frac{\beta - 0.79 - 1/S_h}{\beta - 0.79} \quad (10)$$

From a gas production point of view, this is the worst scenario.

[41] Numerical simulations presented in Figures 4–7 assumed that all the water that resulted from hydrate dissociation is displaced from the pore and that water in initially water-filled pores can be also displaced during gas expansion. Therefore, simulation results show an intermediate efficiency between the values obtained by case 3 (equation (9)) and case 4 (equation (10)). The thin lines in Figures 5a and 7a show the gas recovery efficiency obtained by the general analytical solution (case 1, equation (7)) using the numerically predicted residual gas saturation for each hydrate saturation (Figures 5b and 7b). Analytical results are consistent with the numerical results (There is some discrepancy for the case of low hydrate saturations $S_h < 10\%$ in Figure 5a).

[42] When the initial hydrate saturation exceeds $S_h > 40\%$, gas recovery efficiencies from numerical simulations are similar to case 3 (Figure 8d). In fact, the thick line in Figure 5a is obtained using equation (9). This result shows that when the initial hydrate saturation is high, hydrate-filled pores are interconnected and eventually become a percolating path for gas production. Therefore, gas is produced without the need to invade neighboring water-filled pores during gas expansion, resulting in high gas recovery efficiency.

6. Discussion

6.1. Hydrate Habit in Pores: Ostwald Ripening

[43] We assumed full hydrate occupancy as a starting point for our simulations, in apparent contradiction to some laboratory observations. However, we note that hydrate formation experiments in the laboratory are conducted within relatively short times compared to the long geological time involved in hydrate formation in natural sediments [Tohidi *et al.*, 2001; Katsuki *et al.*, 2006, 2007, 2008]. In fact, pore-scale experiments clearly show a pronounced transient behavior during early hydrate formation, involving formation/dissolution cycles within stability P - T conditions [Jung, 2010].

[44] In long-time conditions, the higher saturation around smaller nuclei promotes diffusion from small nuclei toward larger ones. Therefore a large crystal will tend to grow at the expense of smaller neighboring nuclei (Ostwald ripening). This diffusion-controlled aging process alters the crystal size distribution with time [Myerson, 2002; Salamatin *et al.*, 2003]. For example, data gathered for in situ N_2 and O_2 hydrates in polar ice show the change in crystal size distribution through Ostwald ripening [Pauer *et al.*, 1999;

Uchida et al., 1994; *Salamatin et al.*, 2003]. Our assumption of full pore occupancy reflects Ostwald ripening.

6.2. Macroscale Versus Pore-Scale Analyses

[45] At the macroscale, gas production is determined by the “characteristic curve” of the sediment, i.e., the $(u_g - u_w)$ -vs- S_g trend. This curve depends on pore size distribution and connectivity. Pore-scale models inherently capture this behavior and naturally produce the residual water and gas saturation as a function of pore size distribution, initial hydrate saturation and pore connectivity.

6.3. Field Situations

[46] Our simulations are pressure controlled. Yet, results plotted in terms of the expansion factor β are relevant to gas production by either thermal stimulation or depressurization in the absence of secondary hydrate or ice formation. Likewise, the analytical solution for the recovered gas volume is applicable to both depressurization and thermal stimulation (equations (7)–(10), Figure 8). Note that iso-expansion lines superimpose on the phase boundary, i.e., P - T conditions remain on the phase boundary during volume expansion until all the hydrate mass has dissociated. This study does not capture endothermic dissociation and heat conduction. Therefore, results provide recoverable gas but cannot be used to predict rate.

[47] Results show that fluid expansion factor β determines gas recovery efficiency (all else being constant). Deeper reservoirs will have a higher initial P_0 and will require a higher depressurization $\Delta P = P_0 - P_f$ to attain the same fluid expansion β and gas recovery efficiency. (Note that higher temperatures at depth may support higher production rates.)

[48] Gas recovery efficiency away from the production well should consider the fluid expansion factor as a function of pressure during depressurization, i.e., the distance from the production well in depressurization-based production. Therefore, gas recovery efficiency E is inversely proportional to the distance from the borehole.

6.4. Sediment Internal Stability During Gas Production

[49] Hydrate dissociation in clayey sediments can induce gas-driven fracture formation due to high capillary entry pressures compared to the in situ effective stress σ_3' [*Shin and Santamarina*, 2010]. Let's make an order of magnitude estimation of this condition.

[50] The pore size or separation d between clay particles can be estimated from the sediment specific surface S_s [m^2/g] and porosity n as $d = 2n/[(1-n) \cdot S_s \cdot \rho_m]$ where ρ_m [g/m^3] is the mineral mass density. Then, the Laplacian capillary pressure $P_c = 2\Gamma/d$ can be written as

$$P_c = \frac{2\Gamma}{d} = \Gamma S_s \rho_m \frac{1-n}{n} \quad (11)$$

For example, the sediment in the Krishna-Godavari basin in India has a porosity $n \approx 0.62$ and specific surface $S_s \approx 90 \text{ m}^2/\text{g}$ (see sediment data of *Yun et al.* [2010]), so the capillary entry pressure is $P_c \approx 10 \text{ MPa}$.

[51] An estimate of the effective stress σ_3' starts by recognizing that typical depths for the gas hydrate stability zone in the ocean are shallower than 800 mbsf [*MacDonald*, 1990] (see P - T data compiled in Figure 1). This implies a

maximum horizontal effective stress $\sigma_3' \leq 0.5 \times 8 \text{ MPa} = 4 \text{ MPa}$ expected in marine hydrate-bearing sediments.

[52] These results suggest that hydrate dissociation will induce gas-driven fracture $\sigma_3' < P_c$ even at slow dissociation rates in fine-grained sediments. Gas recovery efficiency in the fracturing regime is beyond the scope of the analysis presented in this manuscript.

6.5. Gas Migration

[53] Let's analyze the gas migration in a single pore due to buoyancy. The ratio between the buoyant force and the capillary resistance is (Bond number - *Pennell et al.* [1996]):

$$B = \frac{F_{\text{buoyancy}}}{F_{\text{capillary}}} = \frac{\Delta\rho g V_p}{2\pi R_{th}\Gamma} = \frac{4\Delta\rho g R_p^2}{3\Gamma} \quad (12)$$

where $\Delta\rho$ is the density difference between gas and fluid, V_p is the volume of pore $V_p = 4\pi R_p^3/3$, and the throat radius R_{th} is half of the pore radius $R_{th} = 0.5R_p$. Buoyancy and capillary resistance are equal, i.e., $B = 1$, when $R_p \approx 2.3 \text{ mm}$ (assumed that $\Delta\rho \approx \rho_w$). Therefore, gas in a single pore will not migrate even in coarse clean sand. However, tall gas clusters can create the buoyancy drive required to allow them to migrate through intermediate grain size sediments without causing sediment instability [*Geistlinger et al.*, 2006; *Santamarina and Jang*, 2010].

7. Conclusions

[54] Proper pressure and temperature, and the availability of methane are required for hydrate formation. Yet, hydrate distribution and saturation in hydrate-bearing sediments are determined by the sediment pore size distribution, connectivity, and spatial variability. These sediment characteristics also affect recoverable gas, the evolution of gas saturation, and the sediment internal stability during production.

[55] Pore network models permit the study of recoverable gas using a minimal set of pore-scale parameters. Pore network simulation results can guide the selection of physically meaningful parameters for capillary pressure functions and relative permeability equations adopted in FEM simulations.

[56] There is a pronounced hydrate-to-fluid volume expansion across the hydrate phase boundary. Additional expansion occurs during heating and depressurization after dissociation. Gas expansion is hindered in fine-grained sediments due to capillarity in small pores.

[57] A simple close form approximation can be derived for the expansion factor β using the modified ideal gas law. The hydrate-to-fluid volume expansion is primarily determined by the final fluid pressure imposed on the boundary P_f . A given depressurization $\Delta P = P_o - P_f$ will cause higher fluid volume expansion in shallower reservoirs with lower initial pressure P_o .

[58] The recoverable gas increases with gas expansion and with hydrate saturation. There is very low gas recovery in hydrate-bearing sediments with low hydrate saturation ($S_h < \sim 5\sim 10\%$), even when high gas expansion conditions are imposed.

[59] The effect of pore size on gas recovery efficiency vanishes when the mean pore size is larger than $1 \mu\text{m}$. A mean pore size smaller than $1 \mu\text{m}$ limits the gas recovery efficiency because small pore throats cause high capillary

pressures, limit gas expansion, and lead to capillary trapping. However, highly conductive gas-driven fractures may form in fine-grained sediments and facilitate gas migration.

[60] Gas recovery efficiency, defined as the ratio between the recovered and the initial mass of gas, can be estimated using macroscale analytical solutions verified against numerical results:

$$\frac{\beta - 0.79 - 1/S_{hyd}}{\beta - 0.79} \leq E \leq \frac{\beta - 1.79}{\beta - 0.79}$$

where β is the fluid expansion factor and S_{hi} is the initial hydrate saturation. The gas recovery efficiency approaches the upper estimate when the hydrate saturation exceeds $S_{hyd} > 40$. In water limited systems, the recoverable gas approaches

$$E = \frac{\beta - 1}{\beta - 0.79}.$$

[61] **Acknowledgments.** Support for this research was provided by DOE/NETL Methane Hydrate Project under contract DE-FC26-06NT42963 and the Goizueta Foundation. We are grateful to reviewers for insightful comments.

References

- Al-Futaisi, A., and T. W. Patzek (2003), Extension of Hoshen-Kopelman algorithm to non-lattice environments, *Physica A*, *321*, 665–678, doi:10.1016/S0378-4371(02)01586-8.
- Al-Raoush, R. I., and C. S. Willson (2005), Extraction of physically realistic pore network properties from three-dimensional synchrotron X-ray microtomography images of unconsolidated porous media systems, *J. Hydrol.*, *300*, 44–64, doi:10.1016/j.jhydrol.2004.05.005.
- Anderson, B. J., et al. (2011), Regional long-term production modeling from a single well test, Mount Elbert gas hydrate stratigraphic test well, Alaska North slope, *Mar. Pet. Geol.*, *28*(2), 493–501, doi:10.1016/j.marpetgeo.2010.01.015.
- Boswell, R., D. Sheldner, M. Lee, T. Latham, T. Collett, G. Guerin, G. Moridis, M. Reagan, and D. Goldberg (2009), Occurrence of gas hydrate in Oligocene Frio sand: Alaminos Canyon Block 818: Northern Gulf of Mexico, *Mar. Pet. Geol.*, *26*(8), 1499–1512, doi:10.1016/j.marpetgeo.2009.03.005.
- Collett, T. S., and J. Ladd (2000), Detection of gas hydrate with downhole logs and assessment of gas hydrate concentrations (saturations) and gas volumes on the Blake Ridge with electrical resistivity log data, *Proc. Ocean Drill. Program Sci. Results*, *164*, 179–191, doi:10.2973/odp.proc.sr.164.219.2000.
- Collett, T., et al. (2007), National gas hydrate program expedition 01 initial report, Minist. of Pet. Nat. Gas, Noida, India.
- Dai, S., C. Lee, and J. C. Santamarina (2011), Formation history and physical properties of sediments from the Mount Elbert Gas Hydrate Stratigraphic Test Well, Alaska North Slope, *Mar. Pet. Geol.*, *28*, 427–438.
- Expedition 311 Scientists (2006), Expedition 311 summary, *Proc. Integrated Ocean Drill. Program*, *311*, doi:10.2204/iodp.proc.311.101.2006.
- Expedition 314 Scientists (2009), Expedition 314 Site C0002, *Proc. Integrated Ocean Drill. Program*, *314/315/316*, doi:10.2204/iodp.proc.314315316.114.2009.
- Expedition 316 Scientists (2009), Expedition 316 Site C0006, *Proc. Integrated Ocean Drill. Program*, *314/315/316*, doi:10.2204/iodp.proc.314315316.134.2009.
- Gamwo, I. K., and Y. Liu (2010), Mathematical modeling and numerical simulation of methane production in a hydrate reservoir, *Ind. Eng. Chem. Res.*, *49*, 5231–5245, doi:10.1021/ie901452v.
- Geistlinger, H., G. Krauss, D. Lazik, and L. Luckner (2006), Direct gas injection into saturated glass beads: Transition from incoherent to coherent gas flow pattern, *Water Resour. Res.*, *42*, W07403, doi:10.1029/2005WR004451.
- Hong, H., and M. Pooladi-Darvish (2003), A numerical study on gas production from formations containing gas hydrates, 54th annual technical meeting, Canadian Int. Pet. Conf., Calgary, Alberta, Canada, 10–12 June.
- Hoshen, J., and R. Kopelman (1976), Percolation and cluster distribution. I. Cluster multiple labeling technique and critical concentration algorithm, *Phys. Rev. B*, *14*(8), 3438–3445, doi:10.1103/PhysRevB.14.3438.
- Jung, J. W. (2010), Gas production from hydrate-bearing sediments: Geomechanical implications, Ph.D. thesis, Georgia Inst. of Technol., Atlanta.
- Katsuki, D., R. Ohmura, T. Ebinuma, and H. Narita (2006), Formation, growth and ageing of clathrate hydrate crystals in a porous medium, *Philos. Mag.*, *86*(12), 1753–1761, doi:10.1080/14786430500509062.
- Katsuki, D., R. Ohmura, T. Ebinuma, and H. Narita (2007), Methane hydrate crystal growth in a porous medium filled with methane-saturated liquid water, *Philos. Mag.*, *87*(7), 1057–1069, doi:10.1080/14786430601021652.
- Katsuki, D., R. Ohmura, T. Ebinuma, and H. Narita (2008), Visual observation of dissociation of methane hydrate crystals in a glass micro model: Production and transfer of methane, *J. Appl. Phys.*, *104*, 083514, doi:10.1063/1.3000622.
- Kida, M., et al. (2009a), Natural gas hydrates with locally different cage occupancies and hydrate numbers in Lake Baikal, *Geochem. Geophys. Geosyst.*, *10*, Q05003, doi:10.1029/2009GC002473.
- Kida, M., K. Suzuki, T. Kawamura, H. Oyama, J. Nagao, T. Ebinuma, H. Narita, H. Suzuki, H. Sakagami, and N. Takahashi (2009b), Characteristics of natural gas hydrates occurring in pore-spaces of marine sediments collected from the eastern Nankai trough, off Japan, *Energy Fuels*, *23*, 5580–5586, doi:10.1021/ef900612f.
- Kim, D.-Y., T.-W. Uhm, H. Lee, Y.-J. Lee, B.-J. Ryu, and J.-H. Kim (2005), Compositional and structural identification of natural gas hydrates collected at site 1249 on Ocean Drilling Program Leg 204, *Korean J. Chem. Eng.*, *22*(4), 569–572, doi:10.1007/BF02706645.
- Konno, Y., Y. Masuda, Y. Hariguchi, M. Kurihara, and H. Ouchi (2010), Key factors for depressurization-induced gas production from oceanic methane hydrates, *Energy Fuels*, *24*, 1736–1744, doi:10.1021/ef901115h.
- Kruyer, S. (1958), The penetration of mercury and capillary condensation in packed spheres, *Trans. Faraday Soc.*, *54*(11), 1758–1767, doi:10.1039/tf9585401758.
- Kurihara, M., A. Sato, H. Ouchi, H. Narita, Y. Masuda, T. Saeaki, and T. Fujii (2009), Prediction of gas productivity from eastern Nankai Trough methane hydrate reservoirs, *SPE J.*, *12*, 477–499.
- Lee, C., T.-S. Yun, J.-S. Lee, J. Bahk, and J. C. Santamarina (2010), Geotechnical characterization of marine sediments in the Ulleung basin, *East sea, Eng. Geol.*, *117*, 151–158.
- Lu, H., I. Moudrakovski, M. Riedel, G. Spence, R. Dutrisac, J. Ripmeester, F. Wright, and S. Dallimore (2005), Occurrence and structural characterization of gas hydrates associated with a cold vent field, offshore Vancouver Island, *J. Geophys. Res.*, *110*, B10204, doi:10.1029/2005JB003900.
- MacDonald, G. J. (1990), The future of methane as an energy resource, *Ann. Rev. Energy*, *15*, 53–83.
- McConnell, D., R. Boswell, T. Collett, M. Frye, W. Shedd, G. Guerin, A. Cook, S. Mrozewski, R. Dufrene, and P. Godfriaux (2010a), Gulf of Mexico gas hydrate joint industry project Leg II: Green canyon 955 site summary, Natl. Energy Technol. Lab., Pittsburgh, Pa. (Available at <http://www.netl.doe.gov/technologies/oil-gas/publications/Hydrates/2009Reports/GC955SiteSum.pdf>.)
- McConnell, D., R. Boswell, T. Collett, M. Frye, W. Shedd, G. Guerin, A. Cook, S. Mrozewski, R. Dufrene, and P. Godfriaux (2010b), Gulf of Mexico gas hydrate joint industry project Leg II: Walker Ridge 313 Site summary, Natl. Energy Technol. Lab., Pittsburgh, Pa. (Available at <http://www.netl.doe.gov/technologies/oil-gas/publications/Hydrates/2009Reports/WR313SiteSum.pdf>.)
- Moridis, G. J., and E. D. Sloan (2007), Gas production potential of disperse low-saturation hydrate accumulations in oceanic sediments, *Energy Convers. Manage.*, *48*, 1834–1849, doi:10.1016/j.enconman.2007.01.023.
- Moridis, G. J., M. B. Kowalsky, and K. Pruess (2007), Depressurization-induced gas production from class 1 hydrate deposits, *SPE J.*, *10*, 458–481.
- Moridis, G. J., M. T. Reagan, S.-J. Kim, Y. Seol, and K. Zhang (2009), Evaluation of the gas production potential of marine hydrate deposits in the Ulleung basin of the Korean East Sea, *SPE J.*, *14*(4), 759–781, doi:10.2118/110859-PA.
- Moridis, G. J., S. Silpngarmert, M. T. Reagan, T. Collett, and K. Zhang (2011), Gas production from a cold, stratigraphically bounded gas hydrate deposit at the Mount Elbert gas hydrate stratigraphic test well, Alaska North slope: Implications of uncertainties, *Mar. Pet. Geol.*, *28*, 517–534, doi:10.1016/j.marpetgeo.2010.01.005.
- Myerson, A. S. (2002), *Handbook of Industrial Crystallization*, Butterworth-Heinemann, Boston.

- Nazridoust, K., and G. Ahmadi (2007), Computational modeling of methane hydrate dissociation in a sandstone core, *Chem. Eng. Sci.*, *62*, 6155–6177, doi:10.1016/j.ces.2007.06.038.
- Øren, P.-E., and S. Bakke (2003), Reconstruction of Berea sandstone and pore-scale modelling of wettability effects, *J. Petrol. Sci. Eng.*, *39*, 177–199, doi:10.1016/S0920-4105(03)00062-7.
- Pauer, F., S. Kipfstuhl, W. F. Kuhs, and H. Shoji (1999), Air clathrate crystals from the GRIP deep ice core, Greenland: A number-, size-, and shape-distribution study, *J. Glaciol.*, *45*(149), 22–30.
- Pennell, K. D., G. A. Pope, and L. M. Abriola (1996), Influence of viscous and buoyancy forces on the mobilization of residual tetrachloroethylene during surfactant flushing, *Environ. Sci. Technol.*, *30*, 1328–1335, doi:10.1021/es9505311.
- Ren, Q.-Y., G.-J. Chen, W. Yan, and T.-M. Guo (2000), Interfacial tension of (CO₂ + CH₄) + water from 298 K to 373 K and pressures up to 30 MPa, *J. Chem. Eng. Data*, *45*, 610–612, doi:10.1021/jc990301s.
- Ripmeester, J. A., and C. I. Ratcliffe (1988), Low-temperature cross-polarization/magic angle spinning ¹³C NMR of solid methane hydrates: Structure, cage occupancy, and hydration number, *J. Phys. Chem.*, *92*(2), 337–339, doi:10.1021/j100313a018.
- Ripmeester, J. A., H. Lu, I. L. Moudrakovski, R. Dutrisac, L. D. Wilson, F. Wright, and S. R. Dallimore (2005), Structure and composition of gas hydrate in sediment recovered from the JAPEx/JNOC/GSC et al. Mallik 5L–38 gas hydrate production research well, determined by X-ray diffraction and Raman and solid-state nuclear magnetic resonance spectroscopy, in *Scientific Results From the Mallik 2002 Gas Hydrate Production Research Well Program, Mackenzie Delta, Northwest Territories, Canada*, *Bull. Geol. Surv. Can.*, 585, 106.
- Sachs, W., and V. Meyn (1995), Pressure and temperature dependence of the surface tension in the system natural gas/water Principles of Investigation and the first precise experimental data for pure methane/water at 25°C up to 46.8 MPa, *Colloids Surf. A*, *94*, 291–301, doi:10.1016/0927-7757(94)03008-1.
- Sahimi, M. (1994), *Applications of Percolation Theory*, Taylor-Francis, London.
- Salamatin, A. N., V. Y. Lipenkov, and T. Hondoh (2003), Air-hydrate crystal growth in polar ice, *J. Cryst. Growth*, *257*, 412–426, doi:10.1016/S0022-0248(03)01472-6.
- Santamarina, J. C., and J. Jang (2010), Energy geotechnology: Implications of mixed fluid conditions, International conference on unsaturated soils, Int. Cent. for Numer. Methods in Eng., Barcelona, Spain, 6–8 Sep.
- Seo, Y., H. Lee, and B.-J. Ryu (2002), Hydrate number and two-phase equilibria of CH₄ hydrate in the deep ocean sediments, *Geophys. Res. Lett.*, *29*(8), 1244, doi:10.1029/2001GL014226.
- Shin, H., and J. C. Santamarina (2010), Fluid-driven fractures in uncemented sediments: Underlying particle-level process, *Earth Planet. Sci. Lett.*, *299*, 180–189, doi:10.1016/j.epsl.2010.08.033.
- Shipboard Scientific Party (1990a), Site 796, *Proc. Ocean Drill. Program Initial Rep.*, *127*, 247–322, doi:10.2973/odp.proc.ir.127.106.1990.
- Shipboard Scientific Party (1990b), Background, objectives, and principal results, ODP Leg 127, Japan Sea, *Proc. Ocean Drill. Program Initial Rep.*, *127*, 5–33, doi:10.2973/odp.proc.ir.127.101.1990.
- Shipboard Scientific Party (1991), Site 808, *Proc. Ocean Drill. Program Initial Rep.*, *131*, 71–269, doi:10.2973/odp.proc.ir.131.106.1991.
- Shipboard Scientific Party (1994a), Sites 889 and 890, *Proc. Ocean Drill. Program Initial Rep.*, *146*, 127–239, doi:10.2973/odp.proc.ir.146-1.008.1994.
- Shipboard Scientific Party (1994b), Site 892, *Proc. Ocean Drill. Program Initial Rep.*, *146*, 301–378, doi:10.2973/odp.proc.ir.146-1.010.1994.
- Shipboard Scientific Party (1996a), Site 994, *Proc. Ocean Drill. Program Initial Rep.*, *164*, 99–174, doi:10.2973/odp.proc.ir.164.107.1996.
- Shipboard Scientific Party (1996b), Site 995, *Proc. Ocean Drill. Program Initial Rep.*, *164*, 175–240, doi:10.2973/odp.proc.ir.164.108.1996.
- Shipboard Scientific Party (1996c), Site 997, *Proc. Ocean Drill. Program Initial Rep.*, *164*, 277–334, doi:10.2973/odp.proc.ir.164.110.1996.
- Shipboard Scientific Party (1997), Site 1019, *Proc. Ocean Drill. Program Initial Rep.*, *167*, 353–387, doi:10.2973/odp.proc.ir.167.113.1997.
- Shipboard Scientific Party (1998), Deep Blake-Bahama Outer Ridge, Sites 1060, 1061, and 1062, *Proc. Ocean Drill. Program Initial Rep.*, *172*, 157–250, doi:10.2973/odp.proc.ir.172.105.1998.
- Shipboard Scientific Party (2003a), Site 1244, *Proc. Ocean Drill. Program Initial Rep.*, *204*, 1–132, doi:10.2973/odp.proc.ir.204.103.2003.
- Shipboard Scientific Party (2003b), Site 1251, *Proc. Ocean Drill. Program Initial Rep.*, *204*, 1–119, doi:10.2973/odp.proc.ir.204.110.2003.
- Sloan, E. D., and C. A. Koh (2008), *Clathrate hydrates of natural gases*, 3rd ed., CRC Press, Boca Raton, Fla.
- Soga, K., S. L. Lee, M. Y. A. Ng, and A. Klar (2007), Characterisation and engineering properties of methane hydrate soils, in *Characterisation and Engineering Properties of Natural Soils*, pp. 2591–2642, Taylor-Francis, London.
- Sok, R. M., M. A. Knackstedt, A. P. Sheppard, W. V. Pinczewski, W. B. Lindquist, A. Venkatarangan, and L. Paterson (2002), Direct and stochastic generation of network models from tomographic images: Effect of topology on residual saturations, *Transp. Porous Media*, *46*, 345–371, doi:10.1023/A:1015034924371.
- Stryjek, R., and J. H. Vera (1986), PRSV: An improved Peng-Robinson equation of state for pure compounds and mixture, *Can. J. Chem. Eng.*, *64*, 323–333, doi:10.1002/cjce.5450640224.
- Sum, A. K., R. C. Burruss, and E. D. Sloan (1997), Measurement of clathrate hydrates via Raman spectroscopy, *J. Phys. Chem. B*, *101*(38), 7371–7377, doi:10.1021/jp970768e.
- Tobin, H., M. Kinoshita, J. Ashi, S. Lallemand, G. Kimura, E. J. Screamon, K. T. Moe, H. Masago, and D. Curewitz, and the Expedition 314/315/316 Scientists (2009a), NanTroSEIZE Stage 1 expeditions: Introduction and synthesis of key results, *Proc. Integrated Ocean Drill. Program*, *314/315/316*, doi:10.2204/iodp.proc.314315316.101.2009.
- Tobin, H., M. Kinoshita, and K. T. Moe, and the Expedition 314 Scientists (2009b), Expedition 314 summary, *Proc. Integrated Ocean Drill. Program*, *314/315/316*, doi:10.2204/iodp.proc.314315316.111.2009.
- Tohidi, B., R. Anderson, M. B. Clennell, R. W. Burgass, and A. B. Biderkab (2001), Visual observation of gas-hydrate formation and dissociation in synthetic porous media by means of glass micromodels, *Geology*, *29*, 867–870, doi:10.1130/0091-7613(2001)029<867:VOOGHF>2.0.CO;2.
- Tréhu, A. M., et al. (2004), Three-dimensional distribution of gas hydrate beneath southern Hydrate Ridge: Constrains from ODP Leg 204, *Earth Planet. Sci. Lett.*, *222*, 845–862, doi:10.1016/j.epsl.2004.03.035.
- Tsimpanogiannis, I. N., and P. C. Lichtner (2006), Pore-network study of methane hydrate dissociation, *Phys. Rev. E*, *74*, 056303, doi:10.1103/PhysRevE.74.056303.
- Uchida, T., T. Hondoh, S. Mae, V. Y. Lipenkov, and P. Duval (1994), Air-hydrate crystals in deep ice-core samples from Vostok Station, Antarctica, *J. Glaciol.*, *40*(134), 79–86.
- Uchida, T., T. Hirano, T. Ebinuma, H. Narita, K. Gohara, S. Mae, and R. Matsumoto (1999), Raman spectroscopic determination of hydration number of methane hydrates, *AIChE J.*, *45*(12), 2641–2645.
- Uchida, T., H. Lu, H. Tomaru, and the MITI Nankai Trough Shipboard Scientist (2004), Subsurface occurrence of natural gas hydrate in the Nankai Trough area: Implication for gas hydrate concentration, *Resource Geol.*, *54*(1), 35–44.
- Uddin, M., D. Coombe, D. Law, and B. Gunter (2008), Numerical studies of gas hydrate formation and decomposition in a geological reservoir, *J. Energy Resour. Technol.*, *130*, 032501, doi:10.1115/1.2956978.
- Waite, W. F., et al. (2009), Physical properties of hydrate-bearing sediments, *Rev. Geophys.*, *47*, RG4003, doi:10.1029/2008RG000279.
- Wilder, J. W., et al. (2008), An international effort to compare gas hydrate reservoir simulators, Proceedings of the 6th International conference on gas hydrate, Univ. B. C., Vancouver, B. C., Canada, 6–10 July.
- Wright, J. F., S. R. Dallimore, and F. M. Nixon (1999), Influences of grain size and salinity on pressure-temperature thresholds for methane hydrate stability in JAPEx/JNOC/GSC Mallik 2L–38 gas hydrate research-well sediments, in *Scientific Results From JAPEx/JNOC/GSC Mallik 2L–38 Gas Hydrate Research Well, Mackenzie Delta, Northwest Territories, Canada*, *Bull. Geol. Surv. Can.*, *544*, 229–240.
- Yun, T. S., D. Fratta, and J. C. Santamarina (2010), Hydrate-bearing sediments from the Krishna-Godavari basin: Physical characterization, pressure core testing and scaled production monitoring, *Energy Fuels*, *24*, 5972–5983, doi:10.1021/ef100821t.

J. Jang and J. C. Santamarina, School of Civil and Environmental Engineering, Georgia Institute of Technology, 790 Atlantic Dr., Atlanta, GA 30332, USA. (jjang6@gatech.edu; jcs@gatech.edu)